International Journal of Hydrogen Energy 50 (2024) 333–341

Contents lists available at ScienceDirect

International Journal of Hydrogen Energy

journal homepage: www.elsevier.com/locate/he

Quantitative analysis of local plasticity accompanying hydrogen-related fracture in low-carbon martensitic steel

Xiaodong Lan *, Kazuho Okada, Ivan Gutierrrez-Urrutia, Akinobu Shibata

Research Center for Structural Materials, National Institute for Materials Science, 1-2-1 Sengen, Tsukuba, Ibaraki, 305-0047, Japan

ARTICLE INFO

Handling editor: Dr M Mahdi Najafpour

Keywords:
Hydrogen embrittlement
Martensite
Local plasticity
Electron backscatter diffraction (EBSD)
Digital image correlation (DIC)

ABSTRACT

In this study, the local plasticity accompanying hydrogen-related fracture in a low-carbon martensitic steel was quantitatively investigated by correlative microscopy analysis combining digital image correlation technique and electron backscatter diffraction. The results revealed that strain localization occurred mainly in the bulk of martensite blocks and at prior austenite grain boundaries, both with and without the presence of hydrogen. Moreover, hydrogen enhanced strain localization during deformation and facilitated crack nucleation and propagation. The quantitative analysis showed that the hydrogen-related quasi-cleavage cracking was closely related to the local plastic deformation, and increasing hydrogen content decreased the local strain level required for quasi-cleavage cracking. It was found that strain localization also occurred around the intergranular cracks, suggesting that hydrogen-induced intergranular cracking was not a classical simple decohesion process and strain localization was involved in the sequence of hydrogen-induced intergranular cracking. These findings shed light on the understanding of the intrinsic nature of hydrogen embrittlement.

1. Introduction

Hydrogen as a clean and renewable energy carrier has the potential to significantly reduce greenhouse gases emissions [1,2]. Recently the carbon-free hydrogen-propelled technologies has posed high demands on the development of high-strength steels [3,4]. One example is that the automotive industry is trying to apply high-strength steels to various parts of automobiles in order to reduce CO_2 emissions by reducing the weight of vehicle's body while still meeting strength and ductility requirements [5]. Another example is the use of high-strength steels for the high-pressure hydrogen pipelines and vessels that would be required to underpin hydrogen fuel as a form of energy [6]. However, the production, transportation, and storage of hydrogen can cause severe infrastructure deterioration [7,8], posing a serious impediment for its applications. For example, The absorption of hydrogen by susceptible metals or alloys leads to an abrupt loss of ductility and load-bearing capability [3,9]. This phenomenon, known as hydrogen embrittlement, has been widely recognized and often results in catastrophic and premature failure of structural components even when the stress loading is far below the macroscopic yield strength of the material. Hydrogen embrittlement has thus been an important issue in industrial applications and attracted attention for decades [10]. Martensitic steel is of immense importance for high-strength steels as it is the major strength-providing microstructure [11]. However, martensitic steels are quite susceptible to hydrogen embrittlement [9,12]. The dilemma between strength and hydrogen embrittlement resistance is an intrinsic obstacle to the design and application of high-strength steels operating in hydrogen environments.

To achieve higher resistance to hydrogen embrittlement, it is necessary to understand the fundamental mechanisms of hydrogen embrittlement. Hydrogen-related fracture is often caused by an accelerated crack evolution process involving hydrogen diffusion within the microstructure and interaction with various lattice defects (vacancies, dislocations, and interfaces, etc.) [6]. Lath martensite is a typical microstructure of high-strength low- and medium-carbon steels and consists of a hierarchical microstructure based on the Kurdjumov-Sachs (K–S) orientation relationship between martensite and austenite. Lath martensite comprises several structural units with different length scales: lath, block, packet, and prior austenite grain [13–15]. A lath is a single crystal with a thickness of about 200 nm and contains a high density of dislocations due to the shear deformation associated with martensitic transformation [16]. The boundaries between laths are low-angle boundaries with a misorientation less than 3° [14]. A block consists of many laths having nearly identical crystallographic

* Corresponding author.
E-mail address: LAN.Xiaodong@nims.go.jp (X. Lan).

https://doi.org/10.1016/j.ijhydene.2023.10.273
Received 28 August 2023; Received in revised form 22 October 2023; Accepted 26 October 2023
Available online 8 November 2023

orientation, and a packet consists of several blocks (separated mainly by high-angle boundaries) sharing the same {110} habit plane. A prior austenite grain corresponds to a single grain at austenite state and can be divided into 4 packets, assuming that 24 possible variants are equally present. The large number of high-angle boundaries and high dislocation density are major factors for the high strength of lath martensite [17], which also increase the risk of hydrogen embrittlement. The multi-scale complexity of martensitic microstructures makes it difficult to understand the relationship between hydrogen-related fracture behavior and martensitic microstructures.

Typical modes of hydrogen-related fracture in martensitic steels are quasi-cleavage and intergranular. Hydrogen-related quasi-cleavage fracture is a transgranular fracture that occurs on non-typical cleavage planes [18,19]. Hydrogen-related intergranular fracture occurs along the prior austenite grain boundaries (PAGBs) [20,21]. Several mechanisms have been proposed to account for the hydrogen-related fracture: hydrogen-enhanced localized plasticity (HELP) [22,23], hydrogen-enhanced decohesion (HEDE) [24,25], hydrogen-enhanced and strain-induced vacancies (HESIV) [26]. These embrittlement mechanisms, including their interactions, are well documented in steels. However, the underlying mechanisms for hydrogen-related fracture have not been conclusively elucidated. The multiscale complexity of martensitic microstructures requires scale-bridging analysis to better understand the mechanisms of hydrogen-related fracture. Shibata et al. [21] reported that the hydrogen-related quasi-cleavage fracture propagated parallel to {011} planes inside the lath through precise crystallographic orientation analysis. Considering that {011} planes correspond to slip planes in a body-centered cubic (BCC) structure, plastic deformation would play an important role in quasi-cleavage fracture. Cho et al. [27] reported that the quasi-cleavage fracture of lath martensitic steel involved significant plasticity, evidenced by plastic zones near tear ridges and a high density of dislocations beneath the quasi-cleavage facets. Regarding intergranular fracture in steels, Yamaguchi et al. [28] reported that a small change in grain boundary cohesive energy induced by segregated solute atoms results in several orders of magnitude more energy loss in fracture toughness based on first-principles calculations. One important factor in bridging the gap is energy dissipation by plastic deformation. Although the most common evidence for plasticity is the appearance of slip traces or tear ridges on the intergranular facets [29], these are not sufficient to determine whether the plastic deformation processes are essential for intergranular failure. Wang et al. [30] revealed that the microstructure immediately beneath the intergranular facets of iron exhibited a dislocation cell structure and proposed that hydrogen accelerated the evolution of the dislocation microstructure. To date, however, the role of plasticity in establishing the conditions for hydrogen-related fracture remains controversial. The aim of this study is to extend the understanding on the local deformation behavior in lath martensite, both with and without hydrogen pre-charging. The interplay between cracking, microstructure, and local plasticity will be tracked to provide quantitative information on hydrogen-related fracture.

2. Materials and methods

An Fe-0.2C (wt.%) binary alloy was used in the present study. The detailed chemical composition of the steel is C: 0.21, Si: ≤0.02, Mn: ≤0.02, P: ≤0.005, S: 0.0005, O: 0.0009, N: 0.0008, and Fe: balance (wt. %). The as-received ingot with a thickness of 19.2 mm was cold-rolled to a final thickness of 1.8 mm. The cold-rolled sheets were austenitized at 930 °C for 30 min in vacuum, followed by ice-brine quenching and sub-zero cooling in liquid nitrogen to obtain a fully martensitic structure. Sheet-type single edge notched tensile specimens with a gauge dimension of 10 mm (length) × 5 mm (width) × 1 mm (thickness) were prepared by electrical discharge machining and mechanical polishing. The depth and curvature radius of the notch were 0.75 mm and 0.25 mm, respectively. Both sides of the tensile specimens were mechanically polished to a final thickness of ~1 mm to remove the decarburized layers formed during the heat treatment.

The microstructure of the heat-treated specimen was characterized by optical microscopy and SEM (backscattered electron (BSE) imaging and electron backscatter diffraction (EBSD), Zeiss: Sigma) equipped with a Bruker QUANTAX EBSD system. The specimen surfaces for BSE observations and EBSD measurements were prepared by electrolytic polishing in an electrolyte of 10 % $HClO_4$ and 90 % CH_3COOH, and then mechanically polished with colloidal silica (0.02 μm) to obtain a flat surface. Analysis on the obtained EBSD data was performed using the Bruker QUANTAX ESPRIT software and the TSL OIM analysis software.

The tensile test specimens were pre-charged with hydrogen in an aqueous solution containing 3 % NaCl and 3 g L^{-1} NH_4SCN for 24 h at room temperature. A platinum wire was used as the counter electrode. The total hydrogen content was controlled by changing the hydrogen-charging current density (0.6 A m^{-2} and 1.5 A m^{-2}). Thermal desorption analysis (TDA) was performed using a R-DEC HTDS-004 system equipped with a Q-Mass spectrometer to measure the diffusible hydrogen content (H_D). The TDA was carried out from room temperature to 800 °C at a heating rate of 100 °C h^{-1}. A standard hydrogen leakage system was used for calibration before each measurement. The H_D was determined by measuring the cumulative desorbed hydrogen content from room temperature to 300 °C. Tensile tests were performed at an initial strain rate of 8.3 × 10^{-6} s^{-1} at room temperature. A non-contact digital video extensometer was used to measure tensile elongation. The time interval between the completion of hydrogen charging and the start of TDA measurements or tensile tests was 40 min. The fracture surfaces of the specimens after tensile tests were observed by SEM.

To investigate the relationships between cracking, microstructure features, and strain localization behavior, interrupted tensile tests coupled with *ex-situ* digital image correlation (DIC) analysis were performed. Prior to the hydrogen charging and tensile deformation, crystal orientation mappings around the notch root area of the tensile test specimens were conducted by EBSD with a step size of 0.4 μm. Before tensile deformation, both the uncharged and hydrogen-charged specimens were slightly repolished with colloidal silica, and then etched with a 3 % Nital solution to create microstructure-based speckle patterns. The etched surface features allow a multi-scale (macro-scale and meso-scale) characterization of the deformation response with large field-of-view by *ex-situ* DIC technique. The *ex-situ* microstructure observations before and after deformation were carried out on the same positions as the EBSD measurement using optical microscopy. The optical microscopy images were processed using VIC-2D commercial software to obtain the strain distribution maps.

3. Results

3.1. Microstructure observation and thermal desorption analysis

Fig. 1 shows (a) an optical microscopy image, (b) the corresponding inverse pole figure (IPF) map, and (c) a BSE image of the as-quenched specimen. The colors in the IPF map express the orientations parallel to the normal direction (ND) of the observed section according to the stereographic triangle presented below the IPF map. In the IPF map, the block boundaries, packet boundaries, and PAGBs determined by the orientation analysis are indicated by the black lines, yellow lines, and white dashed lines, respectively. The internal lath structures and PAGB can be observed in the high magnification BSE image (Fig. 1c). The microstructure observation results confirm that the as-quenched specimen exhibits a fully lath martensite structure consisting of blocks and packets inside each prior austenite grain.

Fig. 2 shows typical desorption profiles of the hydrogen-charged specimens obtained by TDA. The H_D of the specimens charged at 0.6 A m^{-2} and 1.5 A m^{-2} were 5.18 wt ppm and 10.2 wt ppm, respectively. The similar shape of the desorption profiles suggests that the hydrogen

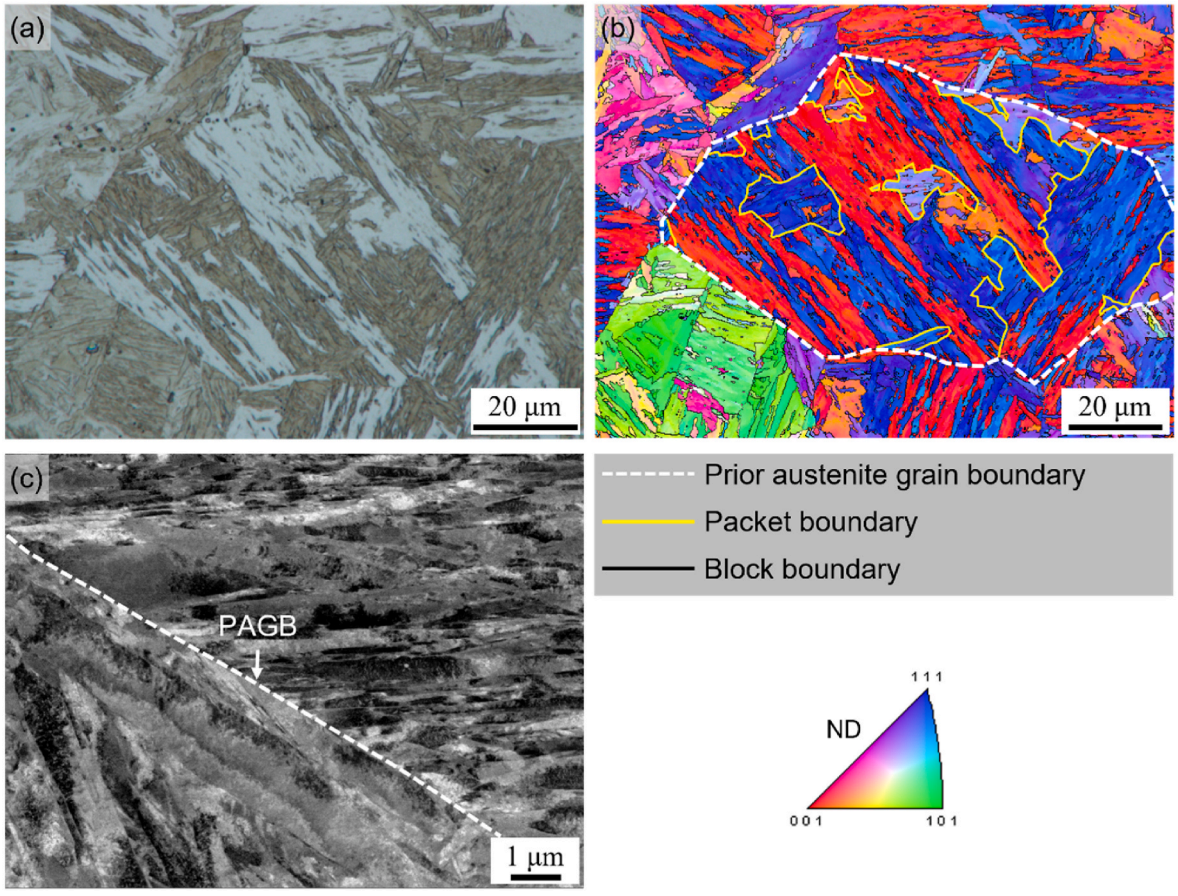

Fig. 1. (a) Optical microscopy image, (b) IPF map of the same area as (a), and (c) BSE image of the as-quenched specimen.

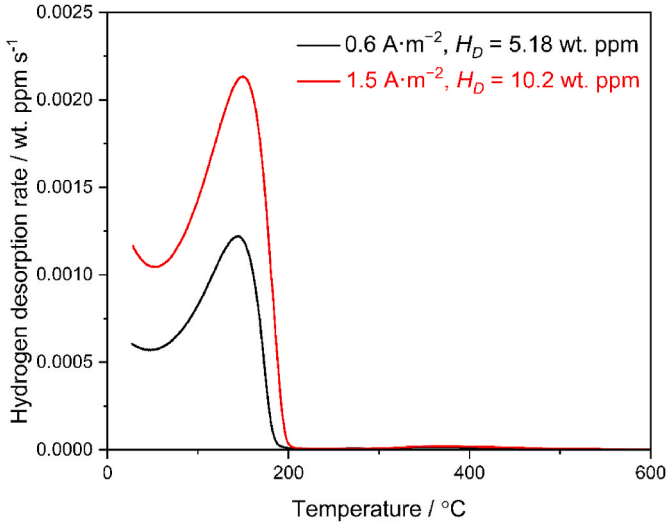

Fig. 2. Desorption profiles of the hydrogen-charged specimens at charging current densities of 0.6 A m^{-2} (black) and 1.5 A m^{-2} (red). (For interpretation of the references to color in this figure legend, the reader is referred to the Web version of this article.)

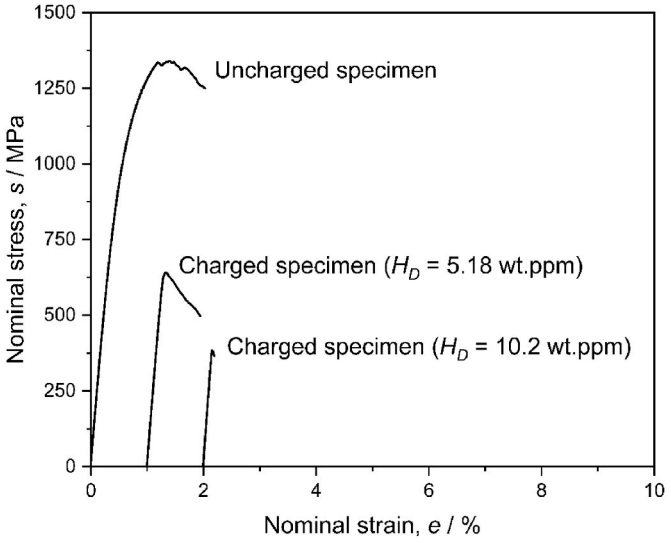

Fig. 3. Nominal stress – nominal strain curves for the uncharged and hydrogen-charged specimens with different H_D.

trapping / distribution behavior did not change when the current density was increased from 0.6 A m^{-2} to 1.5 A m^{-2}.

3.2. Mechanical properties

Fig. 3 presents the nominal stress – nominal strain curves for the uncharged and hydrogen-charged specimens with different H_D. In this study, the nominal stress was calculated from F / A_0, where F is the applied load and A_0 is the initial cross-sectional area at the notch root. The maximum flow stresses are 1341 MPa (uncharged specimen), 641 MPa (hydrogen-charged specimen with H_D = 5.12 wt ppm), and 384 MPa (hydrogen-charged specimen with H_D = 10.2 wt ppm). The fracture strains are 1.4 %, 0.34 %, and 0.16 %, respectively. The uncharged

specimen exhibited some plasticity before fracture, while the hydrogen-charged specimens with $H_D = 5.12$ wt ppm and $H_D = 10.2$ wt ppm were fractured within the apparent elastic regimes. Both the tensile strength and tensile ductility of the specimens decreased significantly with increasing H_D.

Fig. 4 shows SEM images of the fracture surfaces of the uncharged and hydrogen-charged specimens after tensile tests. Fig. 4a–c exhibits the low-magnification SEM images taken immediately beneath the notch root. In the magnified images (Fig. 4d–f), the positions of the typical ductile dimple, quasi-cleavage surface, and intergranular surface are indicated by the white, yellow, and red arrows, respectively. As shown in Fig. 4d, the fracture surface of the uncharged specimen was mainly covered by ductile dimples. In addition to the dimples, some areas of the fracture surface exhibit intergranular fracture features. This is the characteristic of the present martensitic steel, i.e., even in the uncharged state, large stress concentration at the notch root induces brittle intergranular fracture. The fracture surface of the hydrogen-charged specimen with $H_D = 5.18$ wt ppm is composed of ductile dimple, quasi-cleavage surface, and intergranular surface, as shown in Fig. 4e. In the hydrogen-charged specimen with $H_D = 10.2$ wt ppm (Fig. 4f), the fracture morphology shows a large fraction of intergranular surface. The area fraction of intergranular fracture regions increases with increasing H_D.

3.3. Local plastic strain analysis

To investigate the local plastic deformation behavior, interrupted tensile tests coupled with *ex-situ* DIC analysis were performed. Three types of strain were evaluated, i.e., nominal strain e, local strain e_{local}, and average strain e_{avg}. The nominal strain is the macroscopic strain obtained from the non-contact extensometer. The local strain is the micro-level von Mises strain at a specific location obtained from the DIC analysis. The average strain represents the amount of strain in the region of interest by summing up the local strains.

At first, the macroscopic strain distribution map covering a large number of prior austenite grains was analyzed to investigate the effect of hydrogen on the macroscopic strain localization behavior. The uncharged specimen, hydrogen-charged specimens with $H_D = 5.18$ wt ppm, and hydrogen-charged specimens with $H_D = 10.2$ wt ppm were deformed to 0.88 %, 0.89 %, and 0.31 % nominal strain, respectively. The large field-of-view strain distribution maps superimposed on optical microscopy images are presented in Fig. 5. The average strain e_{avg} (as indicated in each figure) of the analyzed area was close to the nominal strain, indicating that the result was reliable. Obviously, strain localization occurred around the notch root in both the uncharged and hydrogen-charged specimens during deformation. We can find that the strain localization was enhanced in the presence of hydrogen (Fig. 5b and c).

In order to determine the positions of strain localization with higher spatial resolution, we analyzed the meso-scale strain distribution map covering several prior austenite grains. Fig. 6 shows (a) the IPF map of the notch root area at the undeformed state, (b) the corresponding optical microscopy image at a nominal strain level of 0.88 %, and (c) the strain distribution map superimposed on the optical microscopy image of the uncharged specimen. The boundaries identified by EBSD analysis are superimposed on the figure, and the black lines and white dashed lines indicate block / packet boundaries and PAGBs, respectively. It was observed that the uncharged specimen was deformed in a highly heterogeneous manner. No cracks were detected at this strain level. The correlative analysis of DIC strain map and IPF map shows that upon deformation, strain localization (elongated 'band-like' morphology) appears in the bulk of the martensite blocks, also particularly at some PAGBs. The deformation bands mainly elongate parallel to the longitudinal direction of the block. The representative strain localization positions in the bulk of the martensite blocks are highlighted by the bold black lines in both the IPF map (Fig. 6a) and the DIC strain map (Fig. 6c).

The correlative analysis results of the hydrogen-charged specimen with $H_D = 5.18$ wt ppm are presented in Fig. 7. At a similar nominal strain level, the hydrogen-charged specimen exhibited enhanced strain localization behavior (Fig. 7c) compared to the uncharged specimen (Fig. 6c). In contrast to the uncharged specimen, many small cracks appeared as indicated by the black lines (Fig. 7c). A major portion of the strain localization exhibits elongated band-like morphology, and these strain-localized regions mainly correspond to the bulk of the blocks and the vicinity of PAGBs. We can find that the cracks tend to form within these strain-localized regions, suggesting that crack initiation requires a certain plastic deformation.

Fig. 8 shows (a) the IPF map obtained before deformation, (b) optical microscopy image showing the crack distribution after deformation, and (c) strain distribution map of the hydrogen-charged specimen with $H_D =$

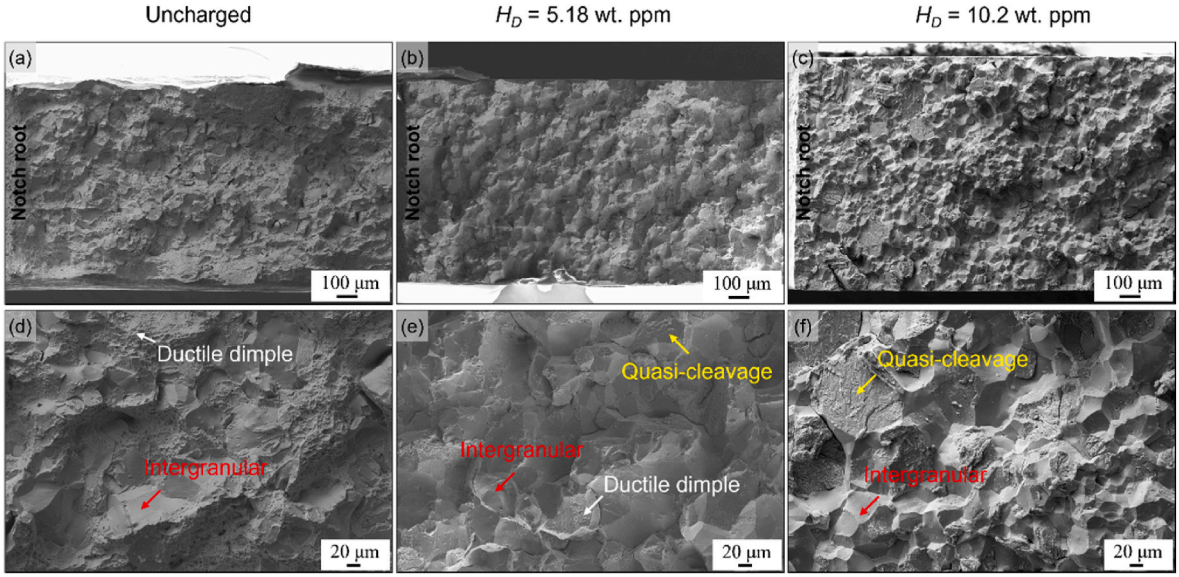

Fig. 4. SEM images showing the fracture surfaces of the (a, d) uncharged specimen, (b, e) hydrogen-charged specimen with $H_D = 5.18$ wt ppm, and (c, f) hydrogen-charged specimen with $H_D = 10.2$ wt ppm. The ductile dimple, quasi-cleavage surface, and intergranular surface are indicated by the white, yellow, and red arrows, respectively. (For interpretation of the references to color in this figure legend, the reader is referred to the Web version of this article.)

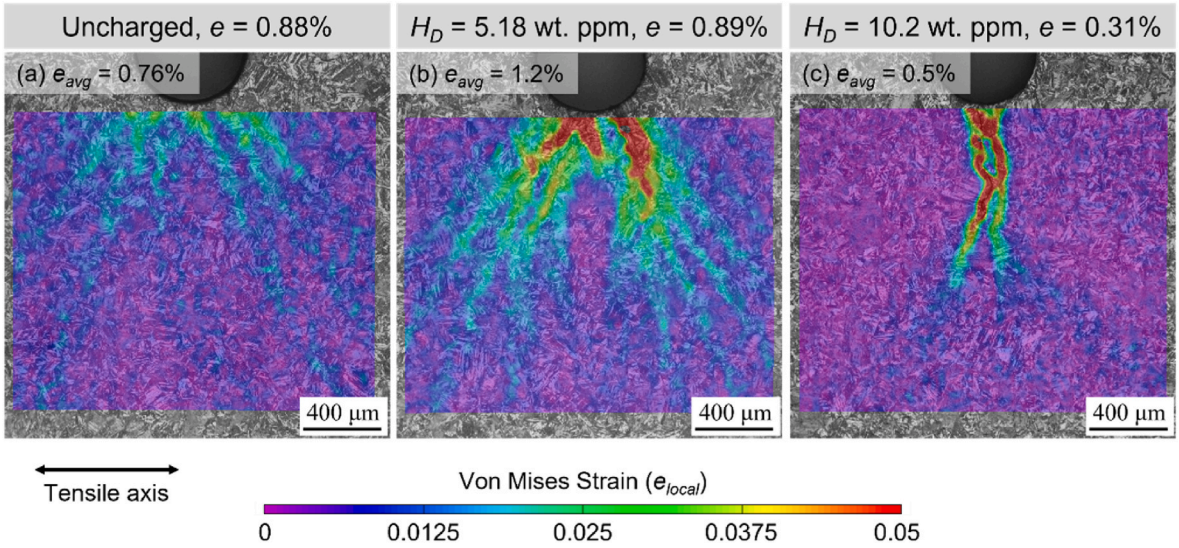

Fig. 5. Large field-of-view strain distribution maps in the specimens with different hydrogen contents (a) uncharged specimen, $e = 0.88$ %, $e_{avg} = 0.76$ %, (b) hydrogen-charged specimen with $H_D = 5.18$ wt ppm, $e = 0.89$ %, $e_{avg} = 1.2$ %, (c) hydrogen-charged specimen with $H_D = 10.2$ wt ppm, $e = 0.31$ %, $e_{avg} = 0.5$ %.

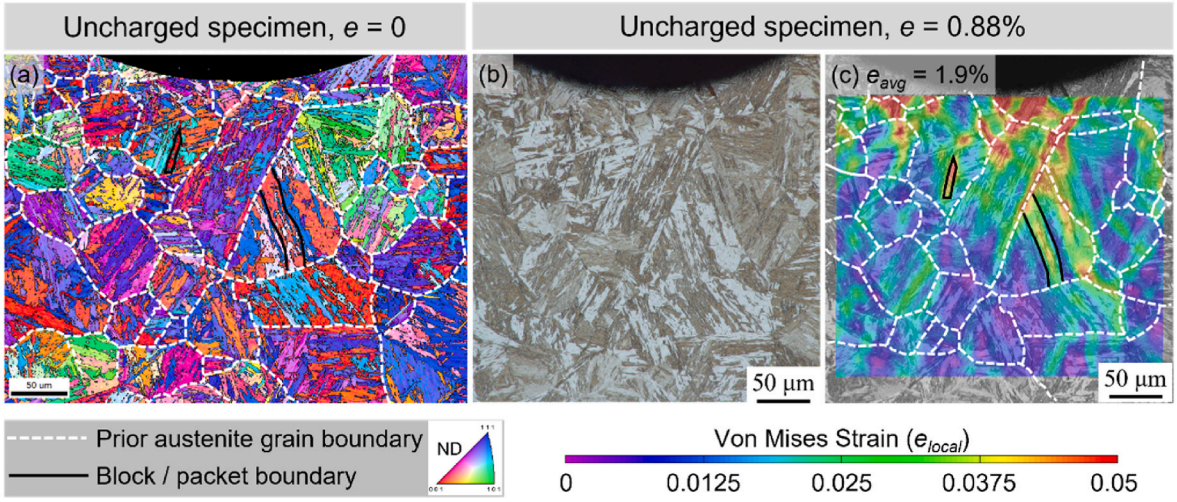

Fig. 6. Results of the correlative analysis for the uncharged specimen at a nominal strain level of 0.88 %. (a) IPF map obtained before deformation, (b) optical microscopy image after deformation, (c) strain distribution map by DIC analysis.

10.2 wt ppm. In Fig. 8b, it can be observed that one large crack formed at the notch root and propagated to the specimen interior. Additionally, a significant number of small cracks also formed. Local plastic deformation was detected even in the apparent elastic strain regime ($e = 0.31$ %). The clear correlation between the cracking sites and the highly deformed regions can be confirmed. The strain mapping analysis correlated with the EBSD crystallographic mapping also revealed that the strain localization was related to microstructures, similar to those observed in Fig. 6c and 7c. From Figs. 6–8, we found that the crack nucleation and growth were enhanced with increasing H_D, even though the nominal strain is much smaller.

The relationship between cracking, microstructure, and local plasticity was quantitatively investigated using local strain profiles, as shown in Fig. 9. The inspection lines (L0 ~ L3) in the strain distribution maps (Fig. 9a and b) represent the locations where the local strain profiles were measured. As shown in Fig. 9c and d, the strain peaks are likely to correspond to the cracked regions or strain-localized regions. The fracture modes (QC for quasi-cleavage and IG for intergranular) of the cracks encountered by the inspection lines are indicated in the corresponding local strain profiles. The results show that the local strain around the quasi-cleavage crack in the hydrogen-charged specimen with $H_D = 10.2$ wt ppm tends to be lower than that in the hydrogen-charged specimen with $H_D = 5.18$ wt ppm. The lower local strain implies that increasing H_D decreases the local strain level required for quasi-cleavage cracking. It is noteworthy that the strain localization also appears around the intergranular cracking, suggesting that the strain localization is also involved in the sequence of intergranular cracking.

4. Discussion

Here we discuss the observed strain localization behavior and the role of local plasticity associated with hydrogen-related fracture. For the uncharged specimen, as shown in Fig. 6c, strain localization occurred mainly in the bulk of the martensite blocks and at some PAGBs, exhibiting distinct characteristics in relation to martensitic microstructure features. For the former, the local deformation bands, which are mainly elongated parallel to the longitudinal direction of the blocks, could be explained by the activation of the in-lath-plane slip system, whose slip direction lies on the lath boundary plane. This observation was in good agreement with previous studies analyzing the characteristics of the slip

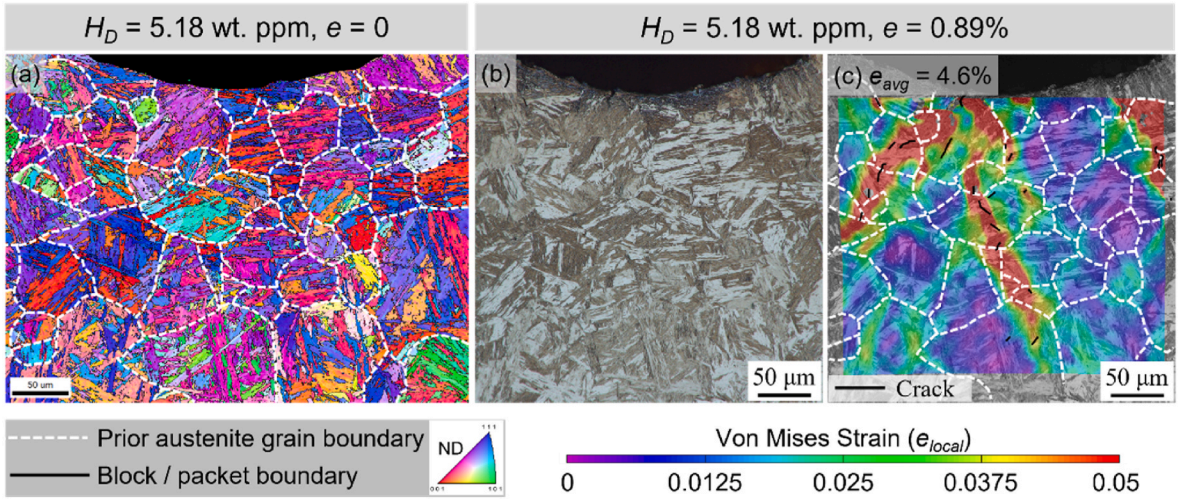

Fig. 7. Results of the correlative analysis for the hydrogen-charged specimen with $H_D = 5.18$ wt ppm at a nominal strain level of 0.89 %. (a) IPF map obtained before deformation, (b) optical microscopy image showing the crack distribution after deformation, (c) strain distribution map by DIC analysis.

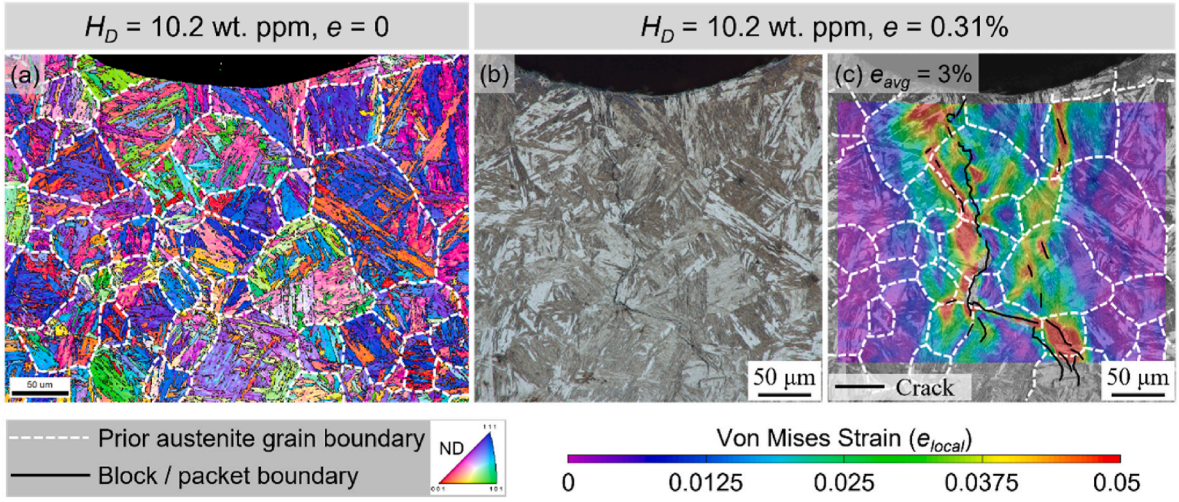

Fig. 8. Results of the correlative analysis for the hydrogen-charged specimen with $H_D = 10.2$ wt ppm at a nominal strain level of 0.31 %. (a) IPF map obtained before deformation, (b) optical microscopy image showing the crack distribution after deformation, (c) strain distribution map by DIC analysis.

system in lath martensite. Michiuchi et al. [31] revealed that the in-lath-plane slip system was preferentially activated compared to the out-of-lath-plane slip system by in-situ EBSD analysis during tensile deformation. Nambu et al. [32] reported that, at strain levels less than the transition strain for out-of-lath-plane slip, slip bands developed parallel to the lath plane in martensite blocks with a large Schmid factor by in-situ tensile test in SEM. Morsdorf et al. [33] revealed that strain localization predominantly occurred along the longitudinal direction of laths oriented at ~45° with respect to the tensile direction during the early stage of deformation. Therefore, the geometrical orientation and crystallographic orientation of the martensite block have superimposed effects on the strain heterogeneity. As for the strain localization at PAGBs, one of the possible reasons is that the incompatibility of transformation strains across the PAGB would enhance local plastic deformation around the PAGB during tensile deformation. In contrast to packet and block boundaries, the character of PAGBs is not determined by the K–S orientation relationship. During the plastic deformation of the lath martensite structure, the geometrical and crystallographic constraints given by the hierarchical microstructures lead to locally inhomogeneous deformation.

For the hydrogen-charged specimens, the DIC results confirmed that hydrogen enhanced strain localization during deformation and that significant local plastic deformation accompanied the quasi-cleavage fracture process. The quantitative analysis shown in Fig. 9 indicated that increasing hydrogen content decreased the local strain level required for quasi-cleavage cracking. Shibata et al. [34] investigated the local conditions for hydrogen-related fracture in a low-carbon martensitic steel and found that the local values of the maximum principal stress, plastic strain, and hydrogen content at the initiation sites of the quasi-cleavage cracks were different depending on the stress concentration factor. Their finite element simulation results are consistent with our experimental results, namely, a higher local hydrogen content results in a lower local strain level for quasi-cleavage cracking. Matsumoto et al. [35] reported that hydrogen reduced the vacancy formation energy and increased the activation energy for vacancy diffusion based on first-principles calculations. They suggested that supersaturated vacancies generated by screw dislocations jog-dragging accumulated in the vicinity of the slip planes and facilitated hydrogen-related cracking during plastic deformation in hydrogen environments. Okada et al. [36] investigated the effect of hydrogen on the evolution of deformation microstructure in a ferritic steel and found that hydrogen increased the relative velocity of screw dislocations to edge dislocations, resulting in

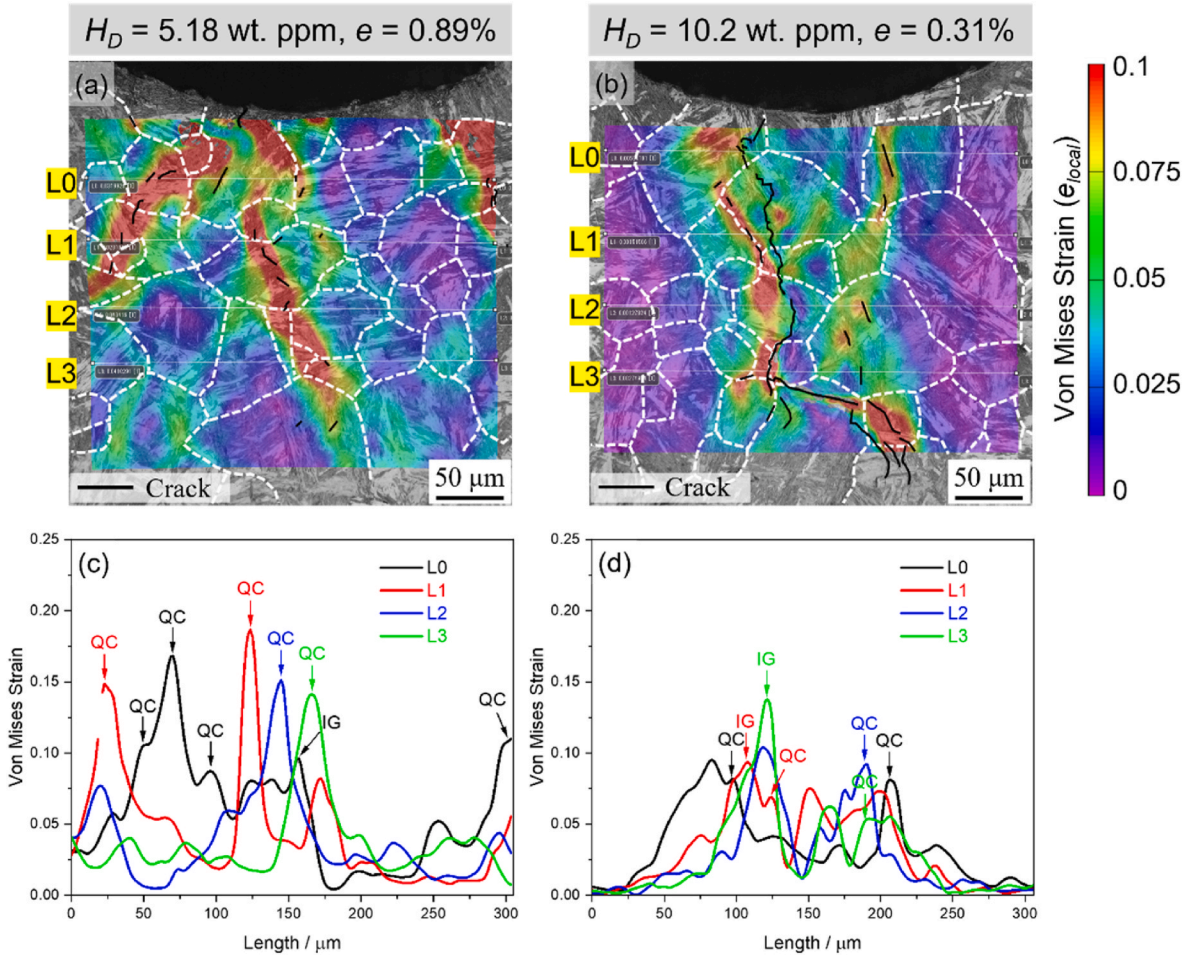

Fig. 9. (a) Strain distribution map and (c) corresponding local strain profiles obtained at $e = 0.89$ % in the hydrogen-charged specimen with $H_D = 5.18$ wt ppm; (b) Strain distribution map and (d) corresponding local strain profiles obtained at $e = 0.31$ % in the hydrogen-charged specimen with $H_D = 10.2$ wt ppm.

the frequent cutting of screw dislocations and tangled dislocation morphology. They proposed that a high density of vacancies was accumulated along the {011} slip planes by jog-dragging of screw dislocations, and coalescence of the accumulated vacancies led to the hydrogen-related quasi-cleavage fracture along the {011} slip planes. Doshida et al. [37] investigated the lattice defect formation using a positron probe microanalyzer and confirmed that the density of vacancies or vacancy clusters in the region near the hydrogen-related quasi-cleavage fracture surface was higher than the other regions in a tempered martensitic steel. Based on the above-referenced studies, the hydrogen-induced reduction in local strain level for quasi-cleavage cracking could be explained by the following mechanism: vacancy multiplication by the jog dragging of screw dislocations is enhanced with increasing hydrogen content, and vacancy diffusion is suppressed by hydrogen, resulting in a high vacancy density in the vicinity of the {011} slip planes; coalescence of these vacancies leads to a hydrogen-related quasi-cleavage fracture at a relatively lower local strain level.

It is well known that increasing hydrogen content can change the fracture mode from quasi-cleavage to intergranular [38]. The classical decohesion model assumes that hydrogen atoms reduce the cohesive energy of the grain boundary and thus induce intergranular cracking. However, in the present study, the meso-scale strain distribution map (Fig. 8c) directly visualized that severe strain localization occurred around intergranular cracks even in the apparent elastic regime, suggesting that hydrogen-induced intergranular cracking was not a simple decohesion process. The plastic deformation processes accompanying hydrogen-assisted intergranular cracking have long been recognized but their role remains unclear. Bechtle et al. [39] observed slip traces on the intergranular fracture facets in hydrogen-charged Ni-201, supporting the idea that plastic deformation plays an important role in hydrogen-induced intergranular fracture. Wang et al. [30] revealed that hydrogen enhanced the development of deformation microstructure beneath the intergranular fracture surface in pure iron and proposed that hydrogen-induced intergranular fracture was a plasticity-mediated process in contrast to the classical decohesion model. Based on first-principles calculations, Yamaguchi et al. [28] found that a small change in grain boundary cohesive energy induced by segregated solute atoms resulted in several orders of magnitude more energy loss in fracture toughness. Energy dissipation by plastic deformation could play an important role in bridging this large gap. These results then raise attentions about the applicability to modify the classical decohesion model to include some plasticity processes. Although the final cracking of PAGBs is a decohesion-based process, we can propose that the precursor strain localization promotes the accumulation of hydrogen at the PAGBs which reduces the grain boundary cohesive energy, and at the same time, establishes a local stress state that could trigger the onset of intergranular cracking.

5. Conclusions

In the present study, the local plasticity accompanying hydrogen-related fracture in as-quenched Fe-0.2C lath martensitic steel was quantitatively investigated by correlative microscopy analysis

combining DIC strain mapping and EBSD crystal orientation mapping. The relationship between cracking, microstructure, and strain localization was tracked, both with and without hydrogen pre-charging. The strain localization and its micromechanical consequences in relation to hydrogen-assisted cracking were discussed. The main findings are summarized as follows:

(1) Upon deformation, strain localization appeared in the bulk of martensite blocks, also particularly at some PAGBs, exhibiting distinct characteristics in relation to martensitic microstructure features. These two types of strain localization were observed in both the uncharged and hydrogen-charged specimens.
(2) The presence of hydrogen enhanced strain localization during deformation and facilitated the nucleation and propagation of cracks. The preferred cracking sites corresponded to the strain localized regions, suggesting that a certain plastic deformation was required for crack initiation and propagation.
(3) The quantitative analysis showed that the quasi-cleavage cracking was closely related to the local plastic deformation. As the hydrogen content increased, the local strain level required for quasi-cleavage cracking decreased.
(4) The strain distribution map directly visualized that strain localization also occurred around the intergranular cracks, suggesting that hydrogen-induced intergranular cracking was not a classical simple decohesion process and strain localization was involved in the sequence of hydrogen-induced intergranular cracking. We proposed that the strain localization promoted the accumulation of hydrogen at the PAGBs, and at the same time, established a local stress state that induced the onset of intergranular cracking.

Declaration of competing interest

The authors declare that they have no known competing financial interests or personal relationships that could have appeared to influence the work reported in this paper.

Acknowledgments

This work was supported by JST PRESTO (Grant Number JPMJPR2096), JSPS KAKENHI (Grant Numbers JP22K18910, JP23H01717 and JP23K13541), Iketani Science and Technology Foundation (Grant Number 0351190-A), and MEXT Program: Data Creation and Utilization Type Material Research and Development Project Grant Number JPMXP1122684766.

References

[1] Baykara SZ. Hydrogen: a brief overview on its sources, production and environmental impact. Int J Hydrogen Energy 2018;43:10605–14. https://doi.org/10.1016/j.ijhydene.2018.02.022.
[2] Abe JO, Popoola API, Ajenifuja E, Popoola OM. Hydrogen energy, economy and storage: review and recommendation. Int J Hydrogen Energy 2019;44:15072–86. https://doi.org/10.1016/j.ijhydene.2019.04.068.
[3] Raabe D, Tasan CC, Olivetti EA. Strategies for improving the sustainability of structural metals. Nature 2019;575:64–74. https://doi.org/10.1038/s41586-019-1702-5.
[4] Sun B, Lu W, Gault B, Ding R, Makineni SK, Wan D, et al. Chemical heterogeneity enhances hydrogen resistance in high-strength steels. Nat Mater 2021;20:1629–34. https://doi.org/10.1038/s41563-021-01050-y.
[5] Gong P, Turk A, Nutter J, Yu F, Wynne B, Rivera-Diaz-del-Castillo P, et al. Hydrogen embrittlement mechanisms in advanced high strength steel. Acta Mater 2022;223:117488. https://doi.org/10.1016/j.actamat.2021.117488.
[6] Chen Y-S, Lu H, Liang J, Rosenthal A, Liu H, Sneddon G, et al. Observation of hydrogen trapping at dislocations, grain boundaries, and precipitates. Science 2020;367:171–5. https://doi.org/10.1126/science.aaz0122. 80.
[7] Woodtli J, Kieselbach R. Damage due to hydrogen embrittlement and stress corrosion cracking. Eng Fail Anal 2000;7:427–50. https://doi.org/10.1016/S1350-6307(99)00033-3.
[8] Rodoni E, Verbeken K, Depover T, Iannuzzi M. Effect of microstructure on the hydrogen embrittlement, diffusion, and uptake of dual-phase low alloy steels with varying ferrite-martensite ratios. Int J Hydrogen Energy 2023. https://doi.org/10.1016/j.ijhydene.2023.07.061.
[9] Song J, Curtin WA. Atomic mechanism and prediction of hydrogen embrittlement in iron. Nat Mater 2013;12:145–51. https://doi.org/10.1038/nmat3479.
[10] Robertson IM, Sofronis P, Nagao A, Martin ML, Wang S, Gross DW, et al. Hydrogen embrittlement understood. Metall Mater Trans A 2015;46:2323–41. https://doi.org/10.1007/s11661-015-2836-1.
[11] Morsdorf L, Tasan CC, Ponge D, Raabe D. 3D structural and atomic-scale analysis of lath martensite: effect of the transformation sequence. Acta Mater 2015;95:366–77. https://doi.org/10.1016/j.actamat.2015.05.023.
[12] Hirata K, Iikubo S, Koyama M, Tsuzaki K, Ohtani H. First-principles study on hydrogen diffusivity in BCC, FCC, and HCP iron. Metall Mater Trans A 2018;49:5015–22. https://doi.org/10.1007/s11661-018-4815-9.
[13] Morito S, Tanaka H, Konishi R, Furuhara T, Maki T. The morphology and crystallography of lath martensite in Fe-C alloys. Acta Mater 2003;51:1789–99. https://doi.org/10.1016/S1359-6454(02)00577-3.
[14] Morito S, Huang X, Furuhara T, Maki T, Hansen N. The morphology and crystallography of lath martensite in alloy steels. Acta Mater 2006;54:5323–31. https://doi.org/10.1016/j.actamat.2006.07.009.
[15] Shibata A, Miyamoto G, Morito S, Nakamura A, Moronaga T, Kitano H, et al. Substructure and crystallography of lath martensite in as-quenched interstitial-free steel and low-carbon steel. Acta Mater 2023;246:118675. https://doi.org/10.1016/j.actamat.2023.118675.
[16] Morito S, Nishikawa J, Maki T. Dislocation density within lath martensite in Fe-C and Fe-Ni alloys. ISIJ Int 2003;43:1475–7. https://doi.org/10.2355/isijinternational.43.1475.
[17] Ohmura T, Tsuzaki K, Matsuoka S. Nanohardness measurement of high-purity Fe–C martensite. Scripta Mater 2001;45:889–94. https://doi.org/10.1016/S1359-6462(01)01121-6.
[18] Lynch SP. A fractographic study of gaseous hydrogen embrittlement and liquid-metal embrittlement in a tempered-martensitic steel. Acta Metall 1984;32:79–90. https://doi.org/10.1016/0001-6160(84)90204-9.
[19] Martin ML, Fenske JA, Liu GS, Sofronis P, Robertson IM. On the formation and nature of quasi-cleavage fracture surfaces in hydrogen embrittled steels. Acta Mater 2011;59:1601–6. https://doi.org/10.1016/j.actamat.2010.11.024.
[20] Shibata A, Madi Y, Okada K, Tsuji N, Besson J. Mechanical and microstructural analysis on hydrogen-related fracture in a martensitic steel. Int J Hydrogen Energy 2019;44:29034–46. https://doi.org/10.1016/j.ijhydene.2019.09.097.
[21] Shibata A, Momotani Y, Murata T, Matsuoka T, Tsuboi M, Tsuji N. Microstructural and crystallographic features of hydrogen-related fracture in lath martensitic steels. Mater Sci Technol 2017;33:1524–32. https://doi.org/10.1080/02670836.2017.1312210.
[22] Birnbaum HK, Sofronis P. Hydrogen-enhanced localized plasticity—a mechanism for hydrogen-related fracture. Mater Sci Eng, A 1994;176:191–202. https://doi.org/10.1016/0921-5093(94)90975-X.
[23] Robertson IM. The effect of hydrogen on dislocation dynamics. Eng Fract Mech 1999;64:649–73. https://doi.org/10.1016/S0013-7944(99)00094-6.
[24] Oriani RA. Hydrogen embrittlement of steels. Annu Rev Mater Sci 1978;8:327–57. https://doi.org/10.1146/annurev.ms.08.080178.001551.
[25] Hirth JP. Effects of hydrogen on the properties of iron and steel. Metall Trans A 1980;11:861–90. https://doi.org/10.1007/BF02654700.
[26] Nagumo M, Yagi T, Saitoh H. Deformation-induced defects controlling fracture toughness of steel revealed by tritium desorption behaviors. Acta Mater 2000;48:943–51. https://doi.org/10.1016/S1359-6454(99)00392-4.
[27] Cho L, Bradley PE, Lauria DS, Martin ML, Connolly MJ, Benzing JT, et al. Characteristics and mechanisms of hydrogen-induced quasi-cleavage fracture of lath martensitic steel. Acta Mater 2021;206:116635. https://doi.org/10.1016/j.actamat.2021.116635.
[28] Yamaguchi M, Kameda J. Multiscale thermodynamic analysis on fracture toughness loss induced by solute segregation in steel. Philos Mag A 2014;94:2131–49. https://doi.org/10.1080/14786435.2014.906757.
[29] Chen T, Chiba T, Koyama M, Akiyama E, Takai K. Factors distinguishing hydrogen-assisted intergranular and intergranular-like fractures in a tempered lath martensitic steel. Metall Mater Trans A 2022;53:1645–58. https://doi.org/10.1007/s11661-022-06608-2.
[30] Wang S, Martin ML, Sofronis P, Ohnuki S, Hashimoto N, Robertson IM. Hydrogen-induced intergranular failure of iron. Acta Mater 2014;69:275–82. https://doi.org/10.1016/j.actamat.2014.01.060.
[31] Michiuchi M, Nambu S, Ishimoto Y, Inoue J, Koseki T. Relationship between local deformation behavior and crystallographic features of as-quenched lath martensite during uniaxial tensile deformation. Acta Mater 2009;57:5283–91. https://doi.org/10.1016/j.actamat.2009.06.021.
[32] Nambu S, Michiuchi M, Ishimoto Y, Asakura K, Inoue J, Koseki T. Transition in deformation behavior of martensitic steel during large deformation under uniaxial tensile loading. Scripta Mater 2009;60:221–4. https://doi.org/10.1016/j.scriptamat.2008.10.007.
[33] Morsdorf L, Jeannin O, Barbier D, Mitsuhara M, Raabe D, Tasan CC. Multiple mechanisms of lath martensite plasticity. Acta Mater 2016;121:202–14. https://doi.org/10.1016/j.actamat.2016.09.006.
[34] Shibata A, Yonemura T, Momotani Y, Park M, Takagi S, Madi Y, et al. Effects of local stress, strain, and hydrogen content on hydrogen-related fracture behavior in low-carbon martensitic steel. Acta Mater 2021;210:116828. https://doi.org/10.1016/j.actamat.2021.116828.
[35] Matsumoto R, Nishiguchi N, Taketomi S, Miyazaki N. First-principles calculation of hydrogen effects on the formation and diffusion of vacancies in alpha iron: discussion of the hydrogen-enhanced strain-induced vacancy mechanism. J Soc Mater Sci Japan 2014;63:182–7. https://doi.org/10.2472/jsms.63.182.

[36] Okada K, Shibata A, Gong W, Tsuji N. Effect of hydrogen on evolution of deformation microstructure in low-carbon steel with ferrite microstructure. Acta Mater 2022;225:117549. https://doi.org/10.1016/j.actamat.2021.117549.
[37] Doshida T, Suzuki H, Takai K, Oshima N, Hirade T. Enhanced lattice defect formation associated with hydrogen and hydrogen embrittlement under elastic stress of a tempered martensitic steel. ISIJ Int 2012;52:198–207. https://doi.org/10.2355/isijinternational.52.198.
[38] Hagihara Y, Shobu T, Hisamori N, Suzuki H, Takai K, Hirai K. Delayed fracture using CSRT and hydrogen trapping characteristics of V-bearing high-strength steel. ISIJ Int 2012;52:298–306. https://doi.org/10.2355/isijinternational.52.298.
[39] Bechtle S, Kumar M, Somerday BP, Launey ME, Ritchie RO. Grain-boundary engineering markedly reduces susceptibility to intergranular hydrogen embrittlement in metallic materials. Acta Mater 2009;57:4148–57. https://doi.org/10.1016/j.actamat.2009.05.012.